# Standby thermal management system for a kW-class vanadium redox flow battery

Andrea Trovò, Massimo Guarnieri

Department of Industrial Engineering – University of Padua, Via Gradenigo 6/A, 35131, Padova, Italy

Interdepartmental Centre Giorgio Levi Cases for Energy Economics and Technology – University of Padua, Via Gradenigo 6/A, 35131, Padova, Italy

## ABSTRACT

Standby is a condition that may occur several times and for long periods in the operation of a redox flow battery for energy storage services in electrical grids (from a national grid down to smart grids, microgrids, …), so that the efficient operation of these batteries calls for specific standby management procedures, capable of minimizing losses while avoiding solutes precipitation. This paper describes the characteristics of a standby thermal management system capable of performing these tasks with high efficiency. Its design resorts to an experimental and numerical investigation that made use of a cell-resolved dynamic thermal model, determining the stack voltage, self-discharge and temperature evolutions. Two different standby modes were analyzed: one with no electrolyte flow (named "swamped standby mode") and the other with a small electrolyte cooling flow rate (named "streamed standby mode"). In addition, the critical conditions which may lead to V(V) precipitation were identified based on published experimental data. As regards the swamped standby mode, an advanced strategy consisting of smart intermittent washings was designed and tested on a kW-scale vanadium redox flow battery system, showing a dramatic reduction of self-discharge losses compared to a conventional fixed periodic washing. As regards the streamed standby mode, the optimal value of the cooling electrolyte flow rate that minimizes self-discharge was identified. With respect to the swamped one, the streamed standby mode ensures the battery readiness to provide fast power service in safe conditions. To the best of the authors' knowledge, this is the first work in which such thermal management strategy during standby, supported by experimental validation on a kW-class vanadium redox flow battery, is presented.

**Keywords:** electrochemical energy storage, energy management, grid services, thermal management system, vanadium redox flow battery, self-discharge limitation.

# 1 Introduction

Redox flow batteries (RFBs) are expected to play a major role in the expansion of stationary energy storage, in support of renewable energy sources and smart grids, as claimed by several authors [1], [2], [3]. In fact, they can provide a wide number of services, e.g. frequency regulation [4], peak shaving [5], energy arbitrage [6], and others [7], [8], including seasonal storage. The quantity of stored energy is determined by the concentration and volume of reactants in the tanks, while power is determined by the number and size of the cells forming the stack [9]. Consequently, energy and power can be independently sized to meet specific power and energy requirements. The energy storage capacity of existing plants ranges between $10^3$ and $10^8$ Wh, the upper limit being reached by the 200 MW/800 MWh Rongke Power project [10], which exceeds that of all other electrochemical energy storage (ECES) systems, considering that the Hornsdale Power Reserve, i.e. the largest lithium-ion plant in the world, is designed for 100 MW and 185 MWh [11]. At present, the all-vanadium RFB (VRFB), is the flow battery that has achieved the broadest commercial fruition [12], while alternative chemistries are widely studied [13]. Twenty-six companies manufacture VRFBs [14], and several plants exceeding some MW and some MWh have been commissioned, as reported by the global vanadium organization Vanitec [15]. A VRFB uses vanadium/vanadium dissolved in aqueous sulfuric acid in both electrolytes, so that the electrodes and membrane are not cross-contaminated and capacity degradation can be avoided, allowing for unparalleled cycle life and calendar life. The major ions involved are $V^{2+}$, $V^{3+}$, $VO^{2+}$ and $VO_2^+$, which present the oxidation states V(II), V(III), V(IV) and V(V), respectively. In order to increase VRFB performance, research on new materials is underway, e.g. electrolytic solutions [16], [17], membranes [18], [19], and electrodes [20], [21]. These studies, which are typically conduced on small single cells, produced important advancements, but concerns remain on their transferability to industrial-size stacks, made of several large cells [22]. Indeed, the deployment of RFBs at the grid level has been hindered by a perceived limited competitiveness of the technology, because of immature technology and relatively high capital costs [23]. However, some drawbacks do exist, notably the low energy and power densities, the former being due to the limited molar concentration of the ions in the electrolyte and the latter being due to low current density and cell open circuit voltage. High ion concentrations limit the temperature operating range to avoid vanadium ion precipitation [24], [25]. In particular, 1.6 mol $L^{-1}$ vanadium solutions in 5 mol $L^{-1}$ sulfate operate safely at temperatures between 10 °C and 40 °C. Higher temperatures may cause irreversible precipitation of V(V) as

$V_2O_5$ at the positive electrolyte [26], [27] while V(II) may precipitate at the negative electrolyte at low temperatures [28]. A strategy to reduce thermal precipitation consists in using inhibitors in the electrolytes. The effect of additives on the low-temperature stability at the negative compartment was studied by Mousa et al. in [29], and the stabilization of 3 mol $L^{-1}$ vanadium electrolyte in 5 mol $L^{-1}$ sulfate was achieved by Roe et al. by adding 1 wt% $H_3PO_4$ +2 wt% ammonium sulfate at 30 °C [30]. As regards high-temperature stabilization, Kausar et al. [31] have demonstrated that V(V) mixed with 1 wt% $H_3PO_4$ + 2 wt% ammonium sulfate is more stable at 50 °C compared with sodium hexametaphosphate, ammonium sulfate, and ammonium phosphate additives. Zhang et al. [32] carried out a detailed study of the effects of various organic and inorganic additives regarding the stability of V(II), V(III), V(IV) and V(V) ions in sulfuric acid solutions, finding that polyacrylic acid and its mixture with $CH_3SO_3H$ are among the most promising candidates as VRFB electrolyte stabilizing agents. Another strategy to mitigate precipitation issues consists in an efficient control of the electrolyte temperature, and it is attracting an increasing interest, as shown in recent papers by Arenas et al. [33] and Yan et al. [34]. It is worth noting that vanadium salt precipitation must be avoided because it causes energy losses and, even worse, may trigger the occlusion of the cell flow channels, which results in major problems during battery operations or during standby with the pumps turned-off, as reported by Kim et al. [25] and Wei et al. [35]. Standby is an important condition in an energy storage system, which may be requested to stay in rest for long periods, waiting for power in excess to be stored (e.g. from intermittent renewable power supplies) or for power demand from end users to be fulfilled. These issues call for the design of advanced and efficient thermal management systems, capable of keeping the temperature of the battery within safety limits, both during operation and in standby. For these reasons, the thermal management system (TMS) of a VRFB is quite different from TMSs of solid-state batteries, e.g. lead-acid [36], [37] and lithium-ion batteries [38], [39], [40], where, in the latter, the control is devoted to avoid thermal drift, explosion and fire risks. While the development of TMSs for solid-state batteries such as lithium-ion is widely studied, very few papers present similar investigations on industrial-scale VRFBs, the majority of them being cited in the following. Bhattacharjee et al. developed a thermal management control model of a VRFB in MATLAB/Simulink and experimentally validated it in the lab during charge and discharge cycles [41]. It basically operated by varying the electrolyte flow rate so as to pursue optimal energy efficiency while avoiding exceeding the upper temperature limit. Wei et al. proposed a dynamic electro-thermal model that accounts for forced cooling strategies [42]. However, such methods can be

applied only during charging and discharging, when the pumps are turned on and the electrolytes continuously flow through the stack to remove the heat generated therein. Conversely, in standby with no electrolyte flow, a specific control strategy has been disregarded, until now, in the literature, and the problem is usually tackled by emptying the stack to avoid internal heat generation or by continuously circulating the electrolytes at a small fixed flow rate with the consequent energy losses, despite no electrochemical reaction being supplied. Recently, a first paper on this problem was published by Tang et al. who report "Using predictions of stack temperature from the complete thermal model in conjunction with a battery management system, control actions can be carried out. … This might be accomplished, for example, by restarting the pumping system for a short period to circulate the electrolyte between the tanks and stack." [43]. But no implementation of such a smart low-consuming procedure in the battery management system (BMS) of kW-scale VRFB is still documented. In addition, the fast response constitutes an important feature of any battery, as attested by the European Commission in the "2050 Long-term strategy – A Clean Planet for All", reporting: "Different technological solutions compete for storing electricity over timeframes between fractions of seconds and seasons." [44]. In the case of VRFBs, if the stack is emptied during standby, no side reactions occur, so that no critical temperature evolution and self-discharge losses take place, but a battery fast response is prevented because activation is delayed by the time needed to start the pumps and to fill the electrodes of the cells in the stack. On the other hand, VRFBs may offer a "fast" response if the stack is kept filled and the solutions are circulated during standby, as reported by Skyllas-Kazacos et al. [45]. In these conditions, the manufacturer Cell Cube declared reaction times lower than 60 ms for its 10–200 kW VRFBs [46]. This was also stated by the Kansai Electric Power Company (KEPCO), reporting a response time of 350 μs on a kW-scale VRFB system with an exceptional overload capability [47]. Such short delays are necessary in fast grid services, e.g. frequency regulation. This paper aims to fill these gaps, reporting on a new thermal management strategy for standby, that has been implemented and tested in the LabVIEW-based BMS of the 9 kW/27 kWh VRFB test facility IS-VRFB (Industrial-Scale VRFB), in operation in our laboratory. The method presented here allows the aforementioned fast performance at minor techno-economic costs [48]. In particular, two possible operation modes have been conceived and analyzed. In the *swamped standby mode*, the stack is filled with electrolyte and the pumps are turned off. In the *streamed standby mode*, a small constant electrolyte cooling flow rate is applied, at the cost of minor hydraulic losses and somewhat higher self-discharge losses. Thermal precipitation data are

taken from an experimental work by Oboroceanu et al. that analyzes the dependence on temperature and State of Charge (*SOC*) of the induction time that precedes V(V) precipitation [49]. The paper is structured as follows: Section 2 describes the experimental setup. Section 3 summarizes the numerical model capable of predicting the stack thermal evolution in standby. Section 4 describes the investigations on stack voltage, self-discharge losses and cell temperatures obtained in both standby modes implemented in IS-VRFB. In Section 5, the thermal management system is presented, and its capability to thermally control the system while reducing losses in both standby modes is shown. The significance of this work in view of the design of advanced thermal management systems for VRFBs is outlined in the conclusion in Section 6.

**Nomenclature**

| **Symbol** | **Description** |
|---|---|
| **Full symbols** | |
| $A_k$ | cross-sectional area in the *k*-th direction/of *k*-th element |
| $C_j$ | molar concentration for *j*-th vanadium ion |
| $Ch$ | charge |
| $C_P$ | specific heat at constant pressure |
| $C_V$ | total vanadium concentration |
| $Di$ | discharge |
| $E_{0,50}$ | corrected reversible potential at $SOC$ = 50% |
| $E_0$ | reversible potential, open circuit voltage – $OCV$ |
| $F$ | Faraday constant = 96485 C $mol^{-1}$ |
| $I$ | electric current |
| $K$ | universal gas constant = 8.314 J $K^{-1}$ $mol^{-1}$ |
| $l$ | length of resistive segment |
| $M$ | moles |
| $m$ | slope coefficient in the induction time |
| $N$ | number of cells |
| $P$ | power |
| $Q$ | electrolyte flow rate |
| $Q_{cool}$ | cooling stack electrolyte flow rate |

| | |
|---|---|
| $R$ | resistance |
| $S$ | mass source |
| $sd$ | self-discharge |
| $su$ | sulfuric |
| $SOC$ | state of charge |
| $t$ | time |
| $t_{cr}$ | critical time |
| $T$ | temperature |
| $V_s$ | stack voltage |
| $V_t$ | tank volume |
| $V_{els}$ | volume of one electrolyte in the stack |
| $V_{elc}$ | volume of one electrolyte in the half-cell |
| $V(j)$ | $j$-th vanadium ion |
| $z$ | electron number per reaction |
| $\beta$ | concentration coefficient in the induction time |
| $\delta$ | thermal control function |
| $\rho$ | density |
| $\sigma$ | electrical conductivity |
| $\tau$ | induction time |

**Subscripts**

| | |
|---|---|
| − | negative |
| + | positive |
| *air* | room air |
| *c* | cell |
| *co* | crossover |
| *el* | electrolyte |
| *exp* | experimental |
| *fl* | flux |
| *i* | internal |
| *m* | manifold |

| | |
|---|---|
| *n* | *n*-th cell |
| *num* | numerical |
| *re* | cell reaction entropic heat |
| *rel* | relative |
| *s* | stack |
| *su* | sulfuric acid |
| *sd* | self-discharge |
| *sc* | shunt current |
| *st* | standard |
| *t* | tank |
| *tr* | transfer |
| *j* | *j*-th vanadium ion |

## 2 Experimental setup

The IS-VRFB test facility is rated 9 kW/27 kWh and is in operation at the Energy Storage and Conversion Lab of the University of Padua [50], within a research program aimed at advancing the technology for industrial VRFBs. The IS-VRFB stack follows the conventional bipolar plate configuration consisting of 40 cells with a 600 $cm^2$ active area connected hydraulically in parallel and electrically in series. Each cell consists of two 5.7 mm thick (after compression) graphite felt electrodes (Beijing Great Wall, China) and a Nafion® 212 membrane. This stack was tested at current densities up to 665 mA $cm^{-2}$ [51]. The hydraulic circuit for circulating the electrolytes consists of two closed loops connecting the stack with two 550 L tanks containing vanadium solutions with concentration $C_V$ = 1.6 mol $L^{-1}$ in 4.5 mol $L^{-1}$ sulfate. Electrolyte circulation is provided by two magnetic-drive centrifugal pumps, which are powered by two brushless AC motors fed by two variable-frequency inverters capable of modulating the stack electrolyte flow rates based on a feedback signals provided by two flowmeters. The tanks are hermetically sealed, and the residual volumes are filled with inert gas (nitrogen) to prevent vanadium species oxidation from atmospheric oxygen. Flowmeters, differential-pressure sensors, level sensors, resistance temperature detectors (RTDs) and electric probes measure all major thermal, fluid-dynamic and electric quantities (Fig. 1). The *SOC* is computed from the reversible voltage (i.e. the Open Circuit Volage, OCV) $E_0$ that is measured in the small open circuit cell that equips the stack, by means of the Nernst equation, as explained below. More details on the measurement system are provided in [52].

Electric power conditioning during charge/discharge is ensured by the Power Management System (PMS), that consists of an AC/DC bidirectional static converter (Dana, Italy) rated 0−85 V DC and ±75 A DC and is remotely controlled in voltage or current by the BMS. A variable passive load is used for high-current discharges (75–600 A). The BMS controls the experiment and provides measurement processing. It includes a desktop computer with in-house software written in the LabVIEW environment (Fig. 1). Signal interfaces consist of a compact data acquisition device (Compact DAQ NI 9179), optoisolators (Isoblock by Verivolt) and a DC/DC transformer (LEM CV 3-100/SP3). A copper grounding bar provides a common reference to all signals, reducing interferences and noise. The human-machine interface (HMI) of the BMS consists of the synoptic user-friendly front panel made with LabVIEW visual instruments (Fig. 1). An internal subroutine provides temperature management by controlling stack washing cycles according to the implemented procedures.

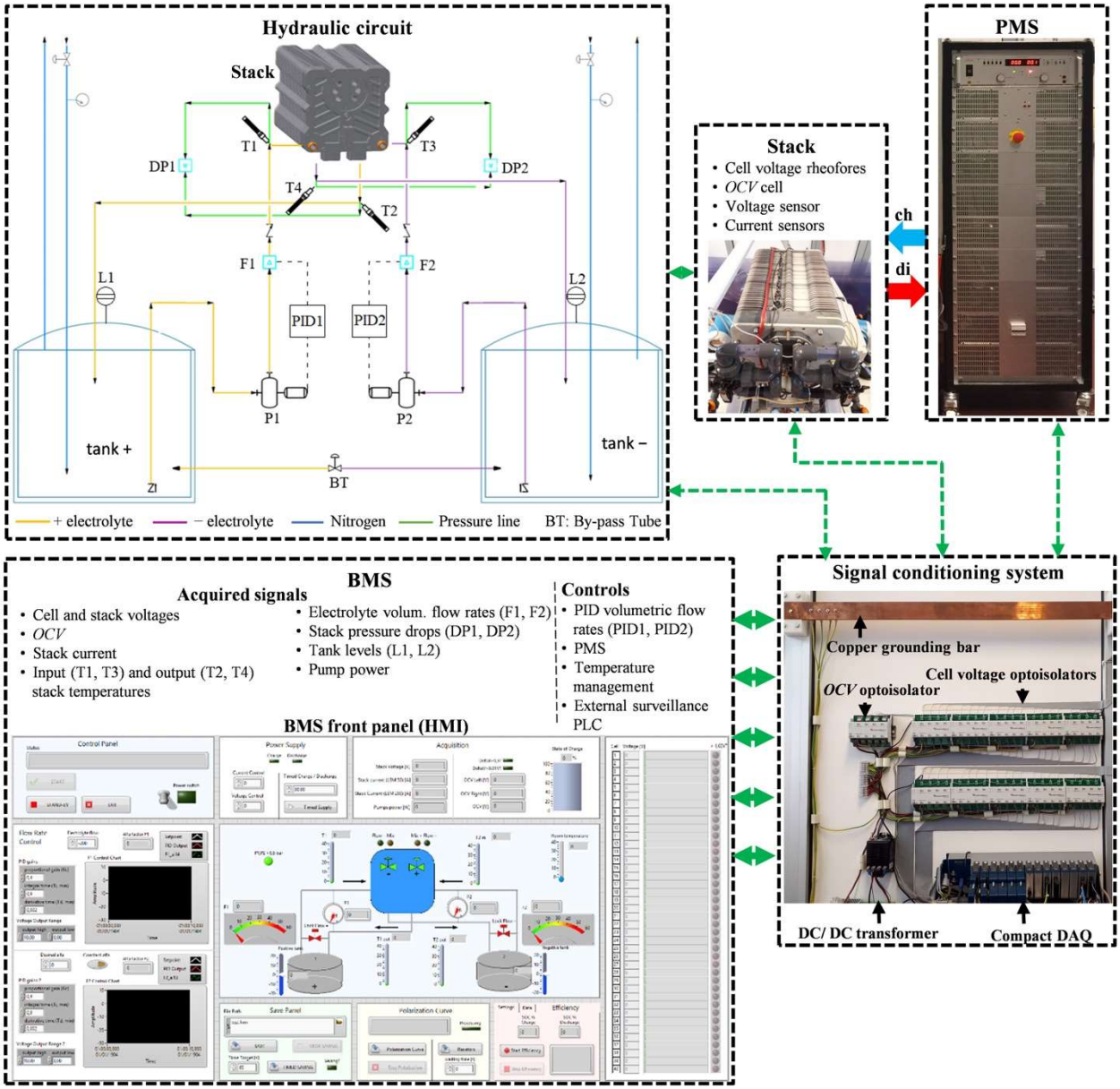


**Fig.1.** The hydraulic scheme of 9 kW/27 kWh IS-VRFB test facility and the scheme of its battery management system, where the thermal control strategy was implemented

## 3 Stack multiphysics model

This section outlines the stack dynamic multiphysics model resolved at cell level that calculates the voltage, temperature and electrolyte concentrations in standby (i.e. with no electric power conversion), with the pumps either turned-off or turned-on. The complete description of the model, including the parameters values used in the simulation performed in this study, is reported in previously published papers, [53], [54]. It must be noted that a limited number of papers has been published so far on the thermal behavior of kW-class VRFBs, notably

[26], [34], 35], [42], [43]. Our model accounts for the losses produced by shunt currents in the stack internal flow paths and for side reactions from vanadium ion crossover through the membrane, resorting to the following assumptions:

- initially, all cells are at the same temperature;
- each half-cell behaves as a double continuous stirred tank reactor, (CSTR) [53] in which the solution is perfectly mixed, so that species concentrations and temperature are uniform inside each cell;
- oxygen and hydrogen evolutions are not considered;
- mass transport of vanadium species through the membrane depends only on diffusion effects, according to Fick's law; and
- all reactions occurring in the cells are instantaneous, once they are permitted by thermodynamic priority in the different standby phases.

During the investigations presented here, a further validation of the model was accomplished by comparing the measured and computed open circuit voltages and self-discharge losses in the stack in the two swamped and streamed standby modes. Hereafter, the first subsection focuses on crossover in the membrane; the second subsection outlines shunt current computation; and in the third subsection, the physical aspects of the standby are described. Finally, the use of the model equations in the BMS procedure is discussed.

### *3.1 Crossover modeling*

Ideally, membranes should be perfectly permeable to protons but impermeable to vanadium ions. However, real membrane experiments crossover, which consists of V(II) (i.e. $V^{2+}$) and V(III) (i.e. $V^{3+}$) ions crossing the membrane from the negative to the positive electrode and of V(IV) (i.e. $VO^{2+}$) and V(V) (i.e. $VO_2^{+}$) ions crossing from the positive to the negative electrode [55], due to electrical effects [56] and concentration gradients [57]. Although crossover does not cause cross-contamination and fast aging in VRFBs, the crossing ions react in the arrival compartment with the ions therein, producing exothermal reactions. The effects are release of heat, decrease of the charged species, and growth of imbalance in electrolyte concentrations and volumes in the two tanks, which result in a loss of capacity [58], [59]. Several studies have been published on the development of new membrane materials capable of reducing crossover without affecting ionic conductivity and durability [60], [61]. However, as long as crossover occurs, it causes exothermal side

reactions, in which the released heat equates to the whole enthalpy of reaction [25] without electrical energy generation but producing self-discharge instead [62]. In the positive compartment, diffusing V(III) and V(II) react with V(IV) and V(V) as [63]:

$$V^{2+} + 2VO_2^+ + 2H^+ \rightarrow 3VO^{2+} + H_2O \quad (1)$$

$$V^{3+} + VO_2^+ \rightarrow 2VO^{2+} \quad (2)$$

$$V^{2+} + VO^{2+} + 2H^+ \rightarrow 2V^{3+} + H_2O \quad (3)$$

Similarly, in the negative compartment, diffusing V(IV) and V(V) react with V(III) and V(II) as:

$$VO^{2+} + V^{2+} + 2H^+ \rightarrow 2V^{3+} + H_2O \quad (4)$$

$$VO_2^+ + 2V^{2+} + 4H^+ \rightarrow 3V^{3+} + 2H_2O \quad (5)$$

$$VO_2^+ + V^{3+} \rightarrow 2VO^{2+} \quad (6)$$

Reactions (3) and (6) only can occur when either V(V) and V(II) are depleted in the positive and negative compartment so that reactions (1) and (2) or (4) and (5) end, respectively.

### *3.2 Shunt current model*

The electrolytes are conductive solutions fed in parallel to homologous electrodes through manifolds and flow channels (Fig. 2), and shunt currents appear in those internal paths, fed by the different electrode electrical potentials [64]. These shunt currents are always present when cells and piping are filled with charged electrolytes, both in standby and load conditions. Shunt currents are a typical lossy side effect of multi-cell stacks. They are typically evaluated by means of equivalent electrical circuits; Fig. 2 shows such a circuit used in this work, with each cell modeled as a Thévenin equivalent made of an ideal voltage source $E_0$ in series with an internal resistance $R_i$. $E_0$ is the cell open circuit voltage ($OCV$) and, with good approximation, corresponds to the cell reversible voltage. Based on the Nernst equation, this reversible voltage can be written as a function of the electrolyte states of charge, which may differ between the two electrolytes $SOC_- = C_{II}/(C_{II} + C_{III})$ and $SOC_+ = C_V/(C_{IV} + C_V)$:

$$E_0 = E_{0,50} + \frac{KT}{F} \ln \frac{SOC_+ SOC_-}{(1 - SOC_+)(1 - SOC_-)} \quad (7)$$

$E_{0,50}$ = 1.37 V is the $E_0$ value at $SOC$ = 50%, $F$ = 96485 C mol$^{-1}$ is the Faraday constant, $z$ = 1 is the number of electrons transferred in the reaction, $K$ = 8.314 J K$^{-1}$ mol$^{-1}$ is the universal gas constant, and $T$ is the absolute temperature. In practice, the lower among $SOC_-$ and $SOC_+$ constitutes the battery $SOC$. It is worth noting that by inverting eq. (7), the expression is derived that allows computing the $SOC$ from the $OCV$ $E_0$ that is measured in the battery's small open-circuit cell:

$$SOC = \frac{e^{(E_0 - E_{0,50})zK/2RT}}{1 + e^{(E_0 - E_{0,50})zF/2KT}} \tag{8}$$

$R_i$ depends on the electrode and membrane materials and sizes, electrolyte $SOCs$ and flow rate and on the operating condition (standby, charge, discharge) [65].

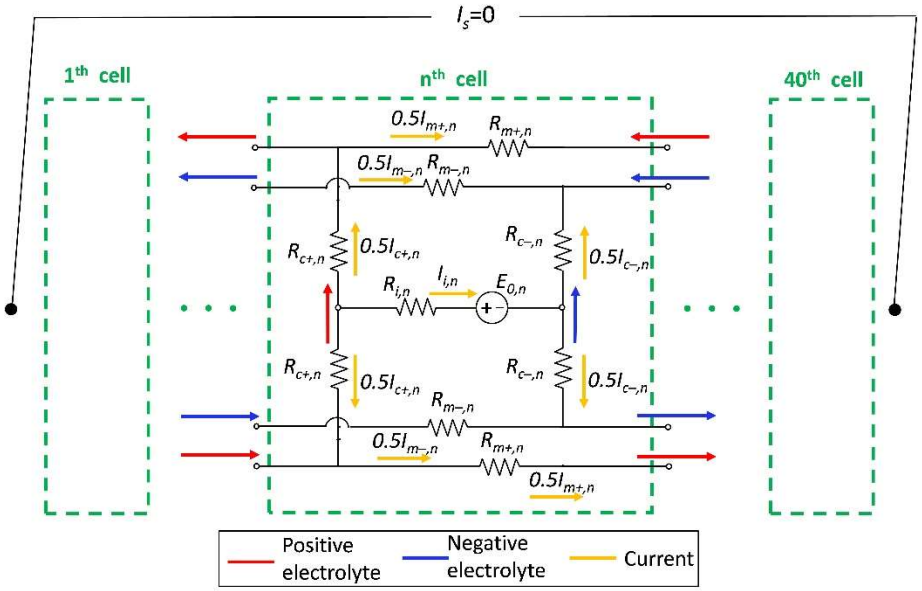


**Fig. 2.** Equivalent electric circuit for calculating stack shunt currents in no-load condition, $I_s$ = 0. Each cell is represented by a Thévenin equivalent, $E_0$ and $R_i$, and the stack hydraulic segments are represented by the resistances $R_k$, i.e. either flow channels $R_c$ or manifolds $R_m$. Electrolyte flows are present only in the streamed standby mode.

The values used in our study were obtained from experimental measurements [54]. The resistances of tubular hydraulic segments $R_k$ with length $l_k$ and cross section $A_k$ were computed as:

$$R_{k\pm} = l_k / \sigma_{\pm}(SOC_{\pm}) A_k \tag{9}$$

where the electrolyte conductivities $\sigma_{\pm}$ depend on the vanadium species concentrations, i.e. on *SOCs*:

$$\begin{cases} \sigma_{+} = SOC_{+}\sigma_{V} + \sigma_{IV}\left(1 - SOC_{+}\right) \\ \sigma_{-} = SOC_{-}\sigma_{II} + \sigma_{III}\left(1 - SOC_{-}\right) \end{cases} \tag{10}$$

The calculation of the electric resistances in the cell compartments (porous electrodes and pertinent flow frames) $R_c$ was determined after a 3-D numerical simulation, made with COMSOL®. Shunt current losses $P_{sc}$ in every circuit segment ($R_i$, $R_c$ $R_m$) were computed as $RI^2$.

### *3.3 Stack standby behavior*

No stack current is present in standby, i.e. $I_s = 0$ in the equivalent circuit, and no electric power conversion occurs, while the pumps may be turned off or on. In both cases, the stack thermal evolution varies according to three phases in which different side reactions occur [53]:

- In *phase 1*, the charged species V(V) and V(II) are present in the pertinent compartments producing the main electrochemical reactions during discharge [66]:

$$\begin{aligned} VO_2^+ + e^- + 2H^+ &\longrightarrow VO^{2+} + H_2O \\ V^{2+} &\longrightarrow V^{3+} + e^- \end{aligned} \tag{11}$$

  which sustain shunt currents. In addition, reactions (1)–(2) and (4)–(5) occur in the positive and negative compartment, respectively, because of species crossover through the membrane [34];
- In *phase 2*, either V(V) in the positive compartment or V(II) in the negative one is depleted, stopping reactions (1)–(2) or (4)–(5) and triggering reaction (3) or (6), respectively, while shunt currents reduce dramatically and become negligible.

  In *phase 3*, both V(V) in the positive compartment and V(II) in the negative one are depleted. In this condition, no electrochemical reactions occur and only V(IV) and V(III) diffuse through the membrane. Shunt currents are negligible, and no significant losses occur.

### *3.4 Mass, energy and thermal model*

In standby, the species mass balance in the cells depends on the species crossover through the membrane and the related side reactions (1)–(6) and on the shunt currents. By modeling the species crossover with Fick's law

and resolving the stack equivalent electric circuit, the mass balance equations for the positive and negative compartments were written as:

$$V_{elc}\frac{dC_{j\pm,n}}{dt} = S_{co,n} + S_{sc,n} + S_{fl,n} \tag{12}$$

where $V_{elc}$ is the electrolyte volume in each half-cell, $C_j$ is the $j = II,\ldots,V$ vanadium species concentration, $S_{co,n}$ is the crossover source contribution, $S_{sc,n}$ is the shunt current source contribution, and $S_{fl,n}$ is the flow rate source contribution. $S_{co,n}$ depends on the membrane properties (i.e. diffusion coefficients of the species and membrane thickness and area). The other source terms on the right-hand side are $S_{sc,n} = I_{i,n}/F$ or $S_{sc,n} = -I_{i,n}/F$ (for $j = II,V$ or $j = III,IV$, respectively) and $S_{fl,n} = Q_{c,+}(C_{j,t+} - C_{j,n+})$ or $S_{fl,n} = Q_{c,-}(C_{j,t-} - C_{j,n-})$ (for $j = IV,V$ or $j = II,III$, respectively). The energy balance equation, allowing to compute the $n$-th cell temperature $T_n$, was written as:

$$\rho C_P V_{elc}\frac{dT_n}{dt} = P_{tr,n} + P_{co,n} + P_{sc,n} + P_{re,n} + P_{fl,n} \tag{13}$$

where $\rho$ and $C_P$ are the density and the specific heat at constant pressure of the electrolyte. On the right-hand side, $P_{tr,n}$ is the heat rate exchanged between the cell and the air, $P_{co,n}$, is the heat rate generated by crossover side reactions (1)–(6), $P_{sc,n}$ is the power losses due to shunt currents, and $P_{re,n}$ is the heat rate due to the main reaction entropy variations [67], which can be neglected during standby due to the very cell low currents. More details are given in [54]. Finally, $P_{fl,n}$ is a further heat rate exchange due to electrolyte circulation, that is zero if the pumps are turned off (swamped standby mode).

# 4 Standby mode analysis

## *4.1 Stack voltage evolution*

The stack voltage profile has been investigated in both standby modes. The analyses resorted to measurements and numerical results from the stack multiphysics model presented in the previous sections. The comparison of stack voltage allowed an additional validation of the model, backing the validation of the temperature profile presented in [53]. It is worth noting that the model predicts the stack voltage only in standby phase 1 when the charged species V(V) and V(II) are present in the cell compartments and the stack can supply power whenever a load is inserted. This behavior is of crucial importance in a number of power-quality grid services, e.g.

frequency regulation, in which the battery is expected to respond in few milliseconds. As numerical simulations confirmed, V(II) is depleted first, putting an end to this phase, whose duration depends first of all on the initial *SOC* and also on the initial stack and room temperatures. For example, phase 1 lasts 1.5 h if the electrolytes in the stack have an initial *SOC* = 95%, and it reduces to 0.45 h if initial *SOC* = 20%, as reported in column two of Table 1. Fig. 3a shows the numerical and experimental data of the IS-VRFB stack in the swamped standby mode, starting from an initial *SOC* = 80% with an initial stack temperature of 29 °C and a constant room temperature of 25 °C. The model successfully predicts the voltage profile with a maximum relative error of 4% throughout standby phase 1. Phase 1 ends when no more V(II) is available in the negative electrodes: experimentally, this event is highlighted by the voltage drop occurring at 1.19 h. On the other hand, numerical simulation showed that the V(II) depleted after 1.3 h, i.e. with a delay of 0.11 h and a relative error of 8.5%, that is a sufficient accuracy for the aim of the present analysis. The duration of this phase is detected from the voltage profiles, which show a sudden drop in the measured voltage after 1.19 h, indicating that no more V(II) is present in the negative half-cells, while the corresponding drop in the computed voltage appears after 1.3 h, i.e. 0.11 h later (with a relative error of 8.5% that is sufficiently small for the aim of the analysis).

**Table 1**

Computed performance of the IS-VRFB stack in two standby modes

| Initial *SOC* [%] | swamped standby mode Duration of phase 1 [h] | streamed standby mode 6 h self-discharge [%] |
|---|---|---|
| 95 | 1.5 | 10.5 |
| 80 | 1.3 | 10.0 |
| 65 | 1.15 | 9.0 |
| 50 | 0.9 | 8.5 |
| 35 | 0.7 | 7.5 |
| 20 | 0.45 | 6.5 |

Swamped standby mode: duration of phase 1 in which both charged species V(II) and V(V) are present and feed the main electrochemical reactions. Streamed standby mode: electrolyte self-discharge over a period of 6 h with a cooling

electrolyte flow rate $Q_{cool}$ = 5 L min$^{-1}$. In both cases, the initial stack temperature is $T_s$ = 29 °C and room temperature is $T_{air}$ = 25 °C.

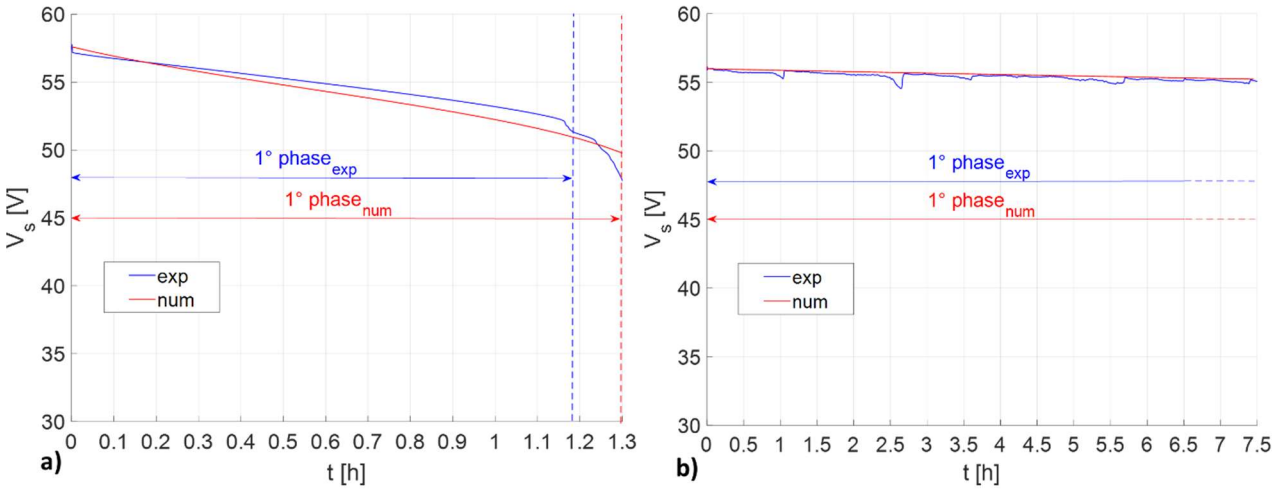


**Fig. 3.** IS-VRFB numerical and experimental stack voltage profiles during standby: ***a)*** swamped standby mode (no flow rate) with initial *SOC* = 80%; ***b)*** streamed standby mode with a cooling flow rate $Q_{cool}$ = 5 L min$^{-1}$ and initial *SOC* = 65%.

In the streamed standby mode, a small constant electrolyte cooling flow rate $Q_{cool}$ = 5 L min$^{-1}$ was applied. Fig. 3b shows the numerical and experimental stack voltage profiles over 7.5 h in the case of an initial *SOC* = 65%, with a discrepancy between experimental and numerical results not exceeding 2%. Similar errors were found applying other initial conditions. The computed stack voltage profiles with different initial *SOCs* in both standby modes are shown in Fig. 4. In the swamped standby mode, the duration of such profiles is limited by the depletion of V(II), that depends on the initial stack *SOC* (voltage profiles stop when V(II) depletes). Conversely, in the streamed standby mode V(II) is always present so that the voltage remains high for longer time. Such plots can be implemented in the BMS to be used in the appropriate standby mode to predict the VRFB electrical performance. Notably, if the battery must be ready to respond quickly and operate for several hours, the streamed mode is preferable. Conversely, if operation time shorter than standby phase 1 is expected, the swamped mode should be selected in order to achieve a better efficiency, because pumping and self-discharge losses are avoided or minimized.

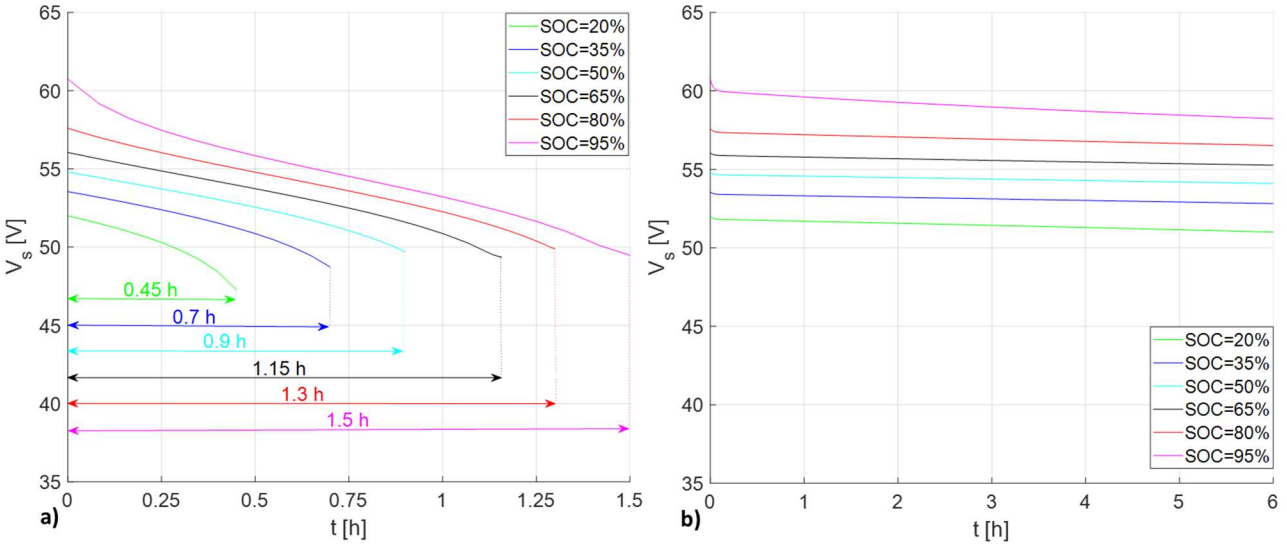


**Fig. 4.** IS-VRFB numerical stack voltage profiles at different initial stack *SOCs* and stack temperatures $T_s$ = 30 °C, ($T_{air}$ = 25 °C): ***a)*** swamped standby mode with no electrolyte flow; ***b)*** streamed standby mode with cooling flow $Q_{cool}$ = 5 L min$^{-1}$.

### *4.2 Self-discharge*

As already stated, a VRFB stack experiences two major side effects during standby, namely species crossover and shunt currents, which result in a loss of energy and battery capacity. Since the active species V(II) and V(V) deplete in phase 1, the charge losses in the swamped standby mode correspond to the initial moles of charged species in the stack: $M_{sd} = SOC_s\ C_V\ V_{els}$ In the case of IS-VRFB, the volume of each electrolyte in the stack is $V_{els}$ = 11 L so that, considering an initial $SOC_s$ = 100%, the maximum charge losses result $M_{sd}$ = 17.6 mol (and they occur in 1.3 h, as shown in Table 1). The charge losses can be put in relation to the charge capacity of the battery:

$$M_{sd,rel} = \frac{M_{sd}}{SOC_t\, C_V\, V_t} = \frac{V_{els}}{V_t} \tag{14}$$

where the last expression holds for $SOC_t = SOC_s$. Under this condition, the previous value yields $M_{sd.rel}$ = 2% in the case of IS-VRFB ($V_t$ = 550 L).

In the streamed standby mode, additional losses are due to the pumping power needed to circulate the electrolytes, and more self-discharge losses are produced by higher species concentration in the cell compartments which cause larger species crossover and higher shunt currents. In this case, standby phase 1

continues without coming to an end, since the charged species are continuously supplied from the tanks into half-cells. Such losses and their duration can also be assessed resorting to heat rate generation, due to self-discharge, as explained in detail in [62], [68]. To this aim, Figs. 5a and 5b show the heat rate generated by the crossover side reactions $P_{co}$ and shunt currents $P_{sc}$ in both standby modes, with an initial $SOC$ = 80%. The total shunt current losses $P_{sc}$ include the contributions of all stack hydraulic segments in the cells and in the internal feeding piping, as already stated. In the case of the swamped standby mode (Fig. 5a), such losses evolve through all three standby phases: the losses in phase 1 are approximately double those in phase 2, while in phase 3 losses are zero, as already stated. Fig. 5b shows the heat rates in the streamed standby mode with a cooling flow rate $Q_{cool}$ = 5 L min$^{-1}$, revealing the permanence of phase 1 during the whole test time (6 hours).

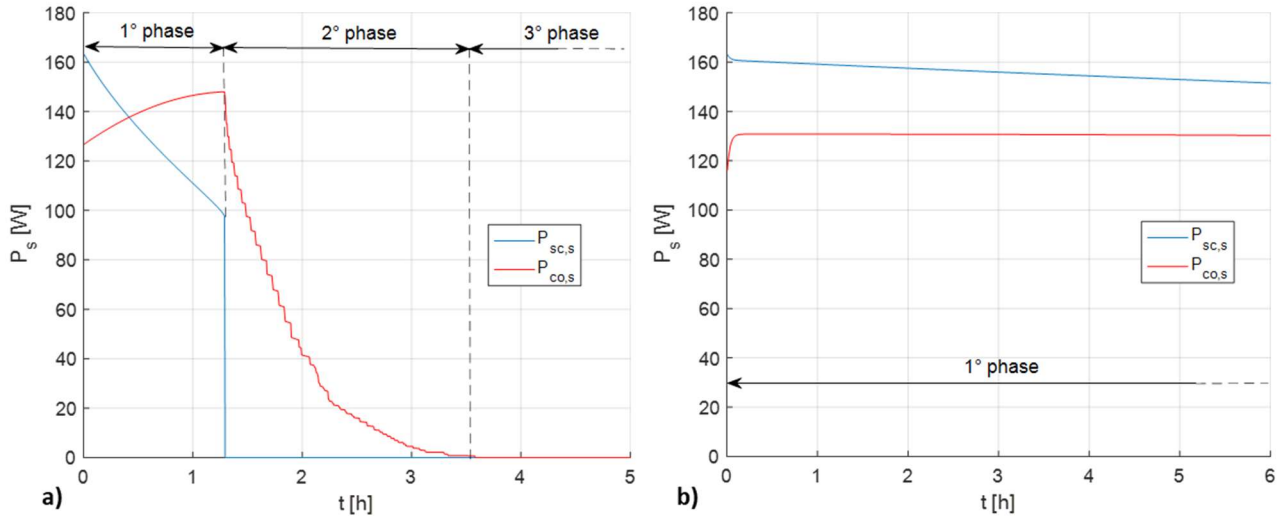


**Fig. 5.** IS-VRFB computed heat rate generated due to shunt currents and crossover side reactions, with initial $SOC$ = 80%, $T_{air}$ = 25 °C, and initial $T_s$ = 30 °C: ***a)*** swamped standby mode, with no flow rate; ***b)*** streamed standby mode, with cooling flow rate $Q_{cool}$ = 5 L min$^{-1}$.

In order to assess the self-discharge losses in the streamed standby mode, a number of simulations of the IS-VRFB behavior over a period of 6 hours with different initial *SOCs* and with a cooling flow rate $Q_{cool}$ = 5 L min$^{-1}$ were carried out. The losses computed under these conditions in the case of six different initial *SOCs* are listed in column three of Table 1. It is shown that, with an initial $SOC$ = 95% and a cooling flow rate $Q_{cool}$ = 5 L min$^{-1}$, the charge losses after 6 hours resulted in 10.5% of the nominal battery charge. Such losses decrease with the initial *SOC*, reducing to 6.5% in the case of an initial $SOC$ = 20%. This effect is due to the lower gradients of active species between the half-cells, which result in a lower vanadium ion crossover and

lower stack open circuit voltage, which is the driving force of shunt currents. Experimental measurements confirmed these self-discharge figures to an accuracy of ±1%. A further validation with $Q_{cool}$ = 10 L min$^{-1}$ over a duration of 15 h provided comparable results, to an accuracy of ±2.5 %.

### *4.3 Thermal behavior*

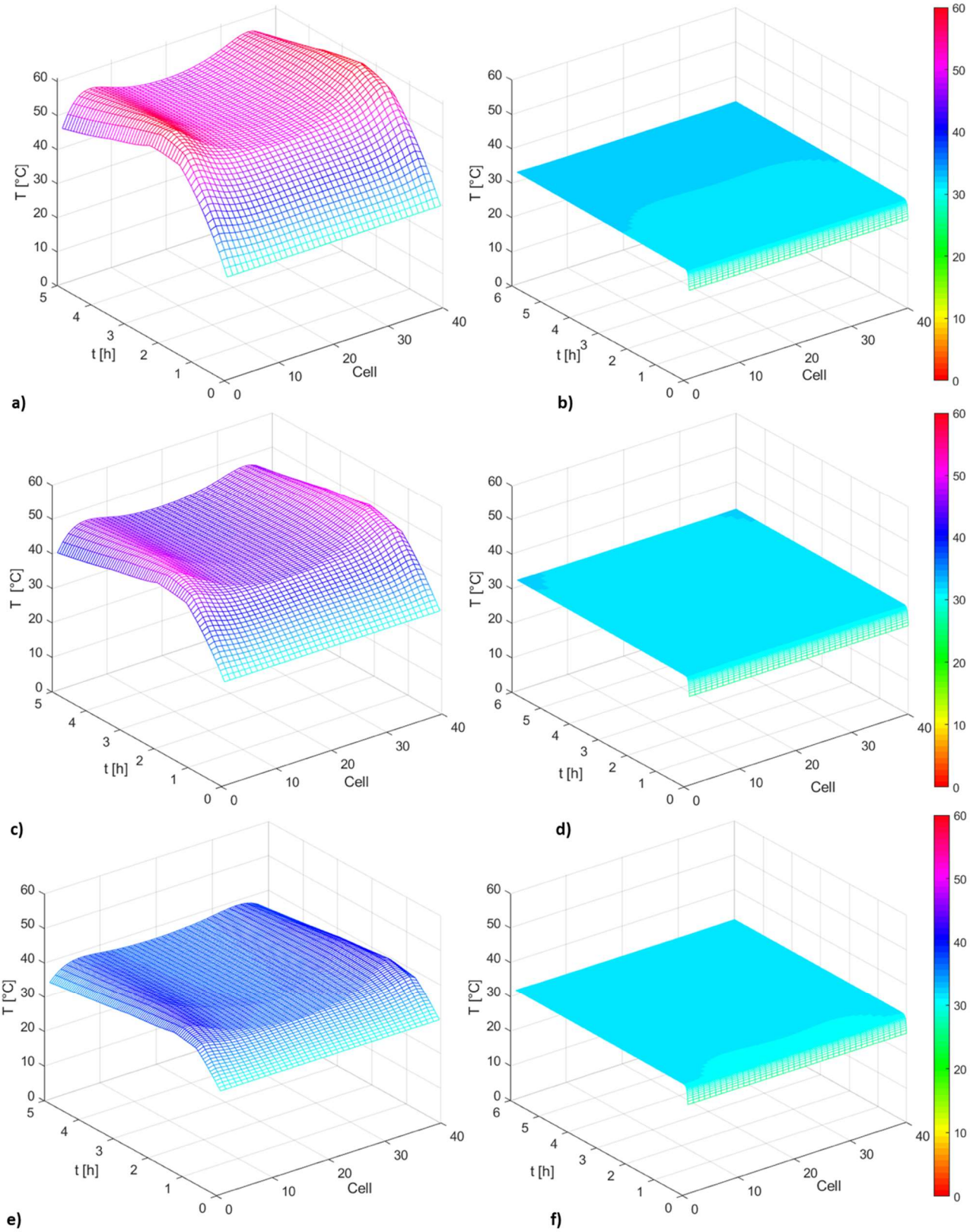


**Fig. 6.** IS-VRFB computed cell temperature distribution, $T_{air}$ = 25 °C, and initial $T_s$ = 29 °C: ***a)***, ***c)***, ***e)*** swamped standby mode with an initial *SOC* = 95%, 65% and 20%, respectively, (with no electrolyte flow); ***b)***, ***d)***, ***f)*** streamed standby mode with an initial *SOC* = 95%, 65% and 20%, respectively, (with an electrolyte flow rate $Q_{cool}$ = 5 L min$^{-1}$).

The stack multiphysics model was used to simulate the thermal behavior of a VRFB stack in the two standby modes, in order to investigate the effect of the electrolyte flow rate $Q_{cool}$ on the cell temperature evolution. Simulations were carried out over a period of 5–6 h, in both standby modes, with an initial stack temperature of 29 °C, which is a conservative values possibly resulting from a previous operation. A room temperature of 25 °C was used, that is a likely value for an outdoor installation in a temperate climate or indoor in an air-conditioned room. Based on the model assumptions, losses occur and heat is generated only during standby phases 1 and 2. Figs. 6a, 6c and 6e show the cell temperature distribution in the swamped standby mode at different initial *SOCs* over a time period of 5 h, that covers phases 1 and 2. Similarly, Figs. 6b, 6d and 6f show the cell temperature distribution in the streamed standby mode for the same initial *SOCs* and in a time period of 6 hours. It can be noted that in the latter case no major evolution occurred on such timescale, since the flow rate $Q_{cool}$ ensured a quick setup of a steady thermal distribution. Conversely, in the swamped standby mode (Figs. 6a, 6c and 6e), large temperature differences among the cells were found, with markedly higher values in the end-cells. This difference is caused by the shunt currents action as detailed elsewhere by Trovò et al. [53], which causes an uneven stack temperature distribution. These differences increase with the initial *SOC*, so that the end-cells reach 60 °C in the case of an initial *SOC* = 95%, an issue that worsens at high room temperature. This effect may promote V(V) precipitation, and in order to prevent it, a smart cooling strategy should be adopted. In the streamed standby mode (Figs. 6b, 6d and 6f), some small differences among the cell still appeared due to uneven cooling and to the heat exchange. However, no significant differences were observed for different initial *SOCs*, and the stack temperatures always remained below 35 °C, i.e. far from critical conditions regarding V(V) precipitation, which reportedly occurs at temperatures not below 40 °C [34].

# 5 Thermal management system

## *5.1 Smart cooling in the swamped standby mode*

A recent study by Oboroceanu et al. evaluated the effect of temperature and species concentration on the positive electrolyte stability [49]. These authors developed an experimental investigation of the induction time after which V(V) precipitation is triggered at different solution concentrations and temperatures. Using those data, they deduced an empirical model of the induction time that was validated in ranges of temperature 30–60 °C, V(V) concentration 1.4–2.2 mol $L^{-1}$, and sulfate concentration 3.6–5.4 mol $L^{-1}$:

$$\tau = \tau_{st} e^{m\left(\frac{1}{T}-\frac{1}{T_{st}}\right)+\beta_{su}\left(C_{su}-C_{su,st}\right)+\beta_V\left(C_V-C_{V,st}\right)} \quad (15)$$

where

- $\tau$ and $\tau_{st}$ are the actual and standard induction times, respectively;
- $C_{su}$ and $C_{su,st}$ = 4.5 mol $L^{-1}$ are the actual and standard concentrations of sulfate, respectively;
- $C_V$ and $C_{V,st}$ = 1.7 mol $L^{-1}$ are the actual and standard concentrations of V(V), respectively;
- $T$ is the absolute electrolyte temperature;
- $m$ is a thermal coefficient; and
- $\beta_{su}$ and $\beta_V$ are concentration coefficients.

For a given VRFB electrolyte, $\tau$ is a function of $C_V$ and $T$. Equation (15) was used in the thermal control algorithm to determine a critical time $t_{cr}$ when a cooling action was needed to avoid precipitation. To this aim, a thermal control function $\delta$ was defined upon which a branch instruction was applied:

$$\delta(0,t) = \int_0^t \frac{1}{\tau(C_V,T)}dt \quad \begin{cases} <1 & \text{no cooling needed} \\ =1 & \text{cooling action required} \end{cases} \quad (16)$$

Equation (16) highlights that the condition $\delta = 1$, as well as the critical time $t = t_{cr}$, depends on $C_V$ and $T$, so they differ from cell to cell. In consequence, the end-cells, where the highest temperatures are found [53], were considered in computing the occurrence of $t_{cr}$ by means of the stack multiphysics model with different initial values of *SOCs*, $T_s$ and $T_{air}$. The results were implemented in a 4-D matrix, which was then used as a look-up table in the real-time computation of the thermal control function $\delta$ with the aim of detecting the shortest critical time $t_{cr}$. Once implemented in a BMS, this algorithm allows to dynamically monitor the need of a cooling action. For the sake of example, if eq. (15) yields an induction time $\tau$ = 1 h at 60 °C and $\tau$ = 2 h at 50 °C, and for any reason the end-cell temperature remains at 50 °C for 1 hour and then jumps to 60 °C, the algorithm dynamically computes the critical time $t_{cr}$ = 1.5 h. The algorithm was implemented and tested in the BMS of IS-VRFB. Whenever the critical time $t_{cr}$ was reached, the BMS activated electrolyte flushes of the tank cooler solutions for 2 min, to fully refresh the electrolyte in the stack, thus reducing the temperature at the cost of minimal losses. The performance of this smart cooling algorithm used in the swamped standby

mode was compared with a conventional procedure consisting of periodic washing at a fixed flow rate and fixed time intervals, e.g. $Q_{cool}$ = 10 L min$^{-1}$ for 2 min every 40 minutes. In IS-VRFB, the 40 min interval corresponds to the time when the maximum temperature is reached in almost all cases, as shown in Figs. 6a, 6c and 6e, so that after this time interval a washing cycle is advisable in the case of a fixed cooling procedure. Figs. 7a and 7b show the resulting battery *SOC* evolution in the case of the conventional and smart cooling modes, respectively. Due to the short duration of the flushes, in both cases the effect of the pumping losses on the battery *SOC* was neglected. Fig. 7a shows that the conventional method involved significant self-discharge losses, namely up to 19% after a 70 h standby period with an initial *SOC* = 40%, due to the quantity of flushed electrolytes, which progressively erodes the global battery state of charge.

Conversely, Fig. 7b shows that the smart method, used in the swamped standby mode, strongly reduces self-discharge losses, especially in the case of a long standby. In particular, in the experiments carried out on IS-VRFB with initial *SOC* ranging between 10% to 95%, initial $T_s \leq 30$ °C and constant $T_{air}$ = 25 °C, $t_{cr}$ was never achieved over periods up to 100 h so that no washing was performed. Consequently, no significant self-discharge losses occurred. It must be said that this behavior is due to the good room heat exchange of IS-VRFB, thanks to its open frame design with the stack located in an open space over the two tanks, that allows an effective heat transfer. Different conditions can occur in compact systems, which present a worse heat exchange. Generally speaking, the smart cooling method prevents unnecessary washing, thus dramatically reducing the number of discharged electrolyte moles. Fig. 7b shows that, even with no cooling action, a small self-discharge occurs, that corresponds to the initial quantity of charged species in the stack which discharge during phase 1. Consistently with eq. (14), in the case of IS-VRFB with an initial *SOC* = 95% in the stack, these losses amount to 1.9% of the battery nominal capacity. When a cooling action is activated, it consists in the refreshing of all the electrolytes contained in the stack so that a charge loss is produced that also is given by eq. (14).

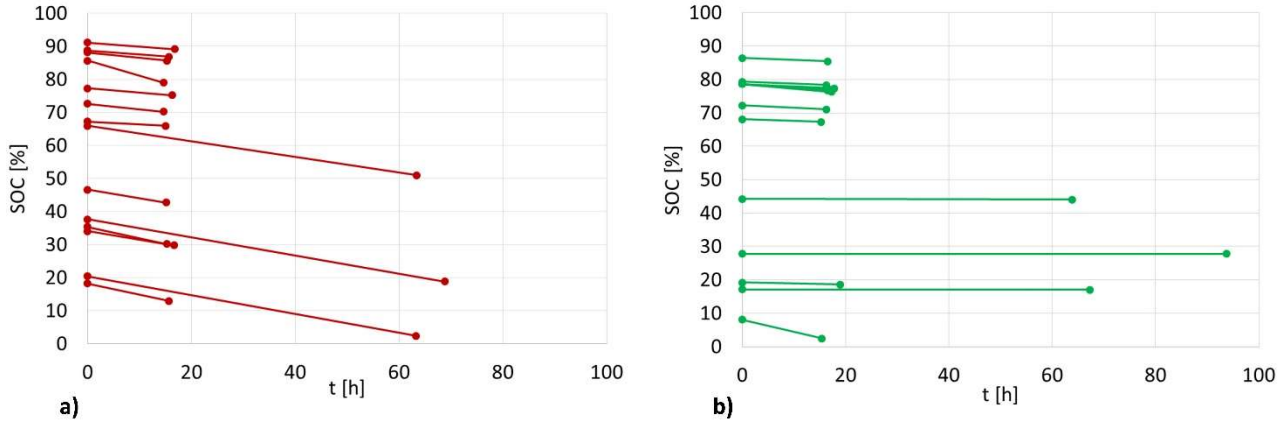


**Fig. 7.** Measured *SOC* self-discharge profiles vs. time in IS-VRFB, during standby: ***a)*** with periodic washing, every 40 min (conventional mode); ***b)*** self-discharge profile vs. time, during standby with the smart control algorithm proposed here.

### *5.2 Smart cooling in the streamed standby mode*

The streamed standby mode, in which a cooling flow rate $Q_{cool}$ is continuously maintained, is less critical from the thermal point of view. In this case, the choice of $Q_{cool}$ depends on four conflicting constraints. Firstly, $Q_{cool}$ must be large enough to avoid stack electrolyte overheating. Secondly, $Q_{cool}$ must be low enough to minimize the V(II) moles lost during standby. Thirdly, $Q_{cool}$ must be large enough to avoid major differences between the electrolyte *SOC* in the stack and tanks, to ensure a prompt and smooth response of the battery at every load request. Fourthly, $Q_{cool}$ must be higher than the minimum pump flow rates (e.g. 3 L $min^{-1}$ in the case of IS-VRFB [65]) but low enough to involve small pumping losses.

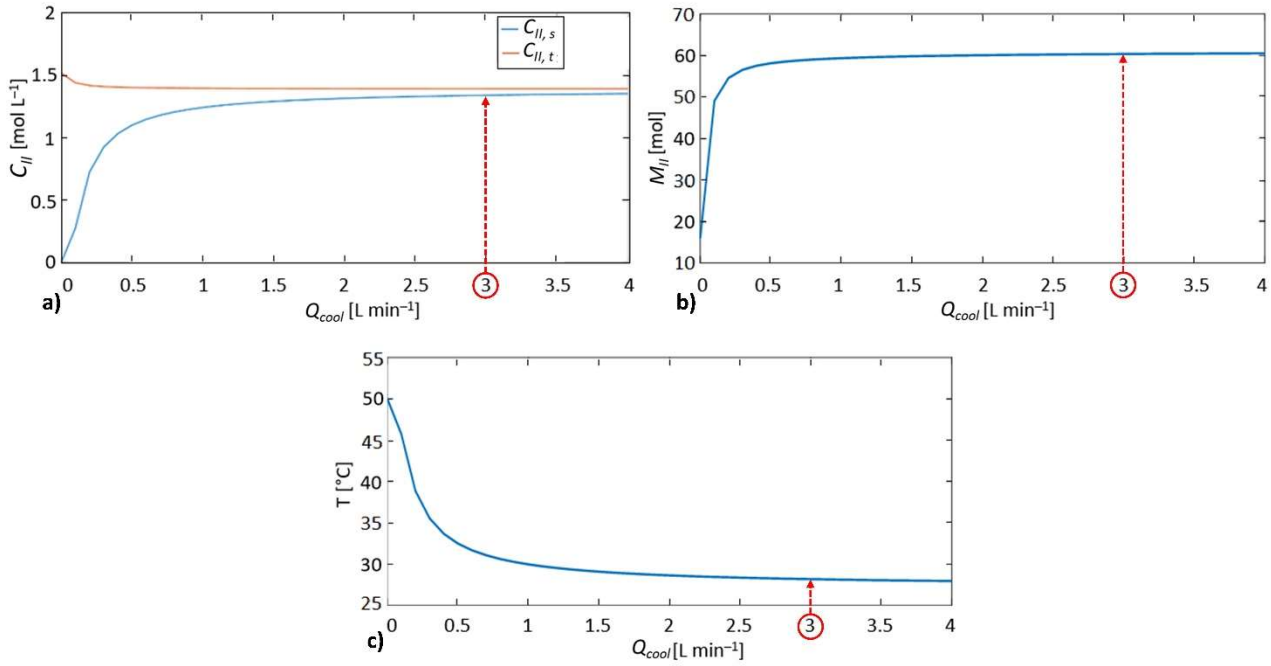


**Fig 8.** IS-VRFB computed conditions in the streamed standby mode after 6 hours with $T_{air}$ = 25 °C at given electrolyte flow rate $Q_{cool}$: ***a)*** V(II) concentration ($C_{II}$) in stack and tanks; ***b)*** V(II) molar losses $M_{II}$; c) average cell temperature $T$.

Keeping into account the previous criteria, the behavior of IS-VRFB in the streamed standby mode was simulated with the stack multiphysics model. The numerical analyses run over 6 hours provided the V(II) concentrations in the stack and in the tank, the V(II) molar losses and the average cell temperature. The computation considered an initial *SOC* (*SOC* = 95%), i.e. the most critical *SOC* condition. The simulations were carried out at different $Q_{cool}$, in order to identify the optimal value matching all previous criteria. Results are shown in Fig. 8: a) stack and tank V(II) concentrations; b) V(II) molar losses; c) average cell temperature. These plots show that $Q_{cool}$ = 3 L min$^{-1}$ is a convenient choice, because it prevents critical cell temperatures, involves almost minimized V(II) losses and allows the stack and tank V(II) concentrations to be fairly equal. By twist of fate, $Q_{cool}$ = 3 L min$^{-1}$ is also the minimal flow rate that can be effectively controlled by IS-VRFB pumps. A final note is that all our investigations showed that no significant differences appeared in the performance of IS-VRFB by increasing the cooling flow rate above $Q_{cool}$ = 2 L min$^{-1}$, as hinted by the profiles of Fig. 8. Consequently, we can deduce that the profiles of Fig. 3b and Fig. 4b, which have been obtained at $Q_{cool}$ = 5 L min$^{-1}$, also stand for $Q_{cool}$ = 3 L min$^{-1}$. In addition, Fig. 8 indicates that a minimal flow rate $Q_{cool}$ = 0.3 L min$^{-1}$ would be sufficient to prevent precipitation in the case of a room temperature of 25 °C. With the

aim to verify the effectiveness of this TMS, after one year of operation and approximately a total working time of 1200 h, the stack was submitted to a maintenance, repair, and operation procedure to check whether any detriment of material or problems regarding V(V) precipitation had arisen from the inspection. No V(V) precipitates as well as any problems during operation were observed. This demonstrates the success of the present TMS in avoiding the problems related to the precipitation of V(V).

## 6 Conclusions

An advanced thermal management system for an experimental 9 kW/27 kWh redox flow battery was developed and successfully implemented in the LabVIEW environment. By resorting to advanced strategies, this system is able to control the stack electrolyte temperature during standby, i.e. in no-load conditions in order to avoid V(V) precipitation and, at the same time, to limit self-discharge losses. Two different standby procedures were developed. In the *swamped standby mode*, the stack was left filled with electrolytes at an initial *SOC* and no flow rate was applied (pumps turned-off). In the *streamed standby mode*, a small constant cooling electrolyte flow rate was applied. Both modes were analyzed experimentally and numerically, by means of a dynamic multiphisics model [53]. The physical quantities taken into account were the stack voltage, self-discharge losses and cell temperatures. The swamped standby mode was able to minimize self-discharge losses and to maximize efficiency, e.g. in the case of an initial *SOC* = 95%, self-discharge losses were 1.9% of the nominal charge capacity over a standby duration of 1.5 h, after which the electrolytes in the electrodes were fully discharged. However, the gradual discharge of the electrolytes contained in the electrodes caused a reduction of the response capability of the battery on the very short timescale (few milliseconds). Moreover, the *swamped standby mode* produces critical thermal conditions which can trigger V(V) precipitation. Conversely, the *streamed standby mode* exhibited higher self-discharge losses, e.g. 10.5% in the case of an initial *SOC* = 95% and electrolyte flow rate of 5 L $min^{-1}$ over a standby of 6 h. However, it ensures full steady-state stack voltage, guaranteeing the fast response of the battery to any power demand. In addition, it raises significant fewer critical thermal issues. In both modes, the critical conditions regarding V(V) precipitation have been considered in terms of induction time, that preceeds precipitation, as published by Oboroceanu et al. [49]. In the case of the swamped standby mode, a smart thermal management protocol was developed and implemented that controls intermittent stack washing, such that dangerous electrolyte temperatures are avoided and, at the

same time, self-discharge losses are much lower than in conventional pre-programmed washing of fixed duration activated at fixed time intervals. In the case of the streamed standby mode, an optimum constant cooling flow rate was identified, that matches different criteria, i.e. ensures a proper stack voltage response while minimizing self-discharge losses and stack temperature increase. No V(V) precipitation nor operation issues were observed over one year, demonstrating the effectiveness of the developed procedures. Both these standby modes are profitable in an industrial-scale vanadium redox flow battery, being able to avoid critical thermal conditions while saving stored energy. Either one or the other can be adopted depending on the requested grid services. The former can be used when a fast response is not needed. In the other case, the latter allows keeping the battery ready to operate when more demanding services are required, e.g. in grid frequency regulation. In both cases, the stack is kept full of electrolytes, thus avoiding triggering oxygen contamination and drying of residual vanadium in the stack components, not to mention longer battery startup times. To the best of the authors' knowledge, this the first work that reports studies of this kind, both experimental and numerical, of a smart standby thermal management successfully implemented in a kW-class vanadium redox flow battery.

## Acknowledgements

This article is part of project "Grid-optimized vanadium redox flow batteries: architecture, interconnection and economic factors" (GUAR_RICERCALASCITOLEVI 20_01) funded by the 2019 Research Program of the Interdepartmental Centre Giorgio Levi Cases for Energy Economics and Technology of University of Padua.

## References

[1] Skyllas-Kazacos M, McCann J F. Vanadium redox flow batteries (VRBs) for medium-and large-scale energy storage. Advances in batteries for medium and large-scale energy storage. Types and Applications Woodhead Publishing Series in Energy 2015. Chapter10: 329–386. Doi: 10.1016/B978-1-78242-013-2.00010-8.

[2] Tiemann P H, Bensmann A, Stuke V, Hanke-Rauschenbach R. Electrical energy storage for industrial grid fee reduction – A large scale analysis. Energ Conver Manage 2020; 208: 112539. Doi: 10.1016/j.enconman.2020.112539.

[3] Amirante R, Cassone E, Distaso E, Tamburrano P. Overview on recent developments in energy storage: Mechanical, electrochemical and hydrogen technologies. Energ Conver Manage 2017; 132:372–387. Doi: 10.1016/j.enconman.2016.11.046.

[4] Lucas A, Chondrogiannis S. Smart grid energy storage controller for frequency regulation and peak shaving, using a vanadium redox flow battery. Int J Elec Power 2016; 80: 26–36. Doi: 10.1016/j.ijepes.2016.01.025.

[5] Bhattacharjee A, Samanta H, Banerjee N, Saha H. Development and validation of a real time flow control integrated MPPT charger for solar PV applications of vanadium redox flow battery. Energ Conver Manage 2018; 171: 1449–1462. Doi: 10.1016/j.enconman.2018.06.088.

[6] Turker B, Klein S A, Komsiyska L, Trujillo J J, Von Bremen L, Kühn M, Busse M. Utilizing a vanadium redox flow battery to avoid wind power deviation penalties in an electricity market. Energ Conver Manage 2013; 76: 1150–1157. Doi: 10.1016/j.enconman.2013.09.014.

[7] Sarkar T, Bhattacharjee A, Samanta H, Bhattacharya K, Saha H. Optimal design and implementation of solar PV-wind-biogas-VRFB storage integrated smart hybrid microgrid for ensuring zero loss of power supply probability. Energ Conver Manage 2019; 191: 102–118. Doi: 10.1016/j.enconman.2019.04.025.

[8] Hosseina M, Bathaee S M T. Optimal scheduling for distribution network with redox flow battery storage. Energ Conver Manage 2016; 121: 145–151. Doi: 10.1016/j.enconman.2016.05.001.

[9] Turker B, Klein S A, Hammer E-M, Lenz B, Komsiyska L. Modeling a vanadium redox flow battery system for large scale applications. Energ Conver Manage 2013; 66: 26–32. Doi: 10.1016/j.enconman.2012.09.009.

[10] Yang ZG. It's big and long-lived, and it won't catch fire: the vanadium redox-flow battery. IEEE Spectrum; 26-Oct-2017. Available at:https://spectrum.ieee.org/green-tech/fuel-cells/its-big-and-longlived-and-it-wont-catch-fire-the-vanadiumredoxflowbattery.

[11] Hornsdale Power Reserve. Expansion Progress Update, https://hornsdalepowerreserve.com.au/expansion-progress-update/; Mar 23, 2020 [accessed 26 August 2020].

[12] Esan O C, Shi X, Pan Z, Huo X, An L, Zhao T S. Modeling and Simulation of Flow Batteries. Adv Energy Mater 2020, 2000758. Doi: 10.1002/aenm.202000758.

[13] Leung P, Shah A A, Sanz L, Flox C, Morante J R, Xu Q, Mohamed M R, Ponce de Léon C, Walsh F C. Recent developments in organic redox flow batteries: a critical review. J Power Sources 2017; 360:243–283. Doi: 10.1016/j.jpowsour.2017.05.057.

[14] Vanitec Transforming Possibilities. Vanadium Redox Flow Battery Company, http://www.vanitec.org/vanadium-redox-flow-battery-vrfb-companies; 2020 [accessed 26 August 2020].

[15] Vanitec Transforming Possibilities. Vanadium Redox Flow Battery (VRFB) technology is increasingly being tested or deployed across the globe, https://willigan.digital/pr/bold-editorial/vanitec/v3/; 2020 [accessed 26 August 2020].

[16] Choi C, Kim S, Kim R, Choi Y, Kim S, Jung H-Y, Yang J H, Kim H-T. A review of vanadium electrolytes for vanadium redox flow batteries. Renew Sust Energ Rev 2017; 69:263–274. Doi: 10.1016/j.rser.2016.11.188.

[17] Roznyatovskaya N V, Roznyatovsky V A, Hohne C C, Fühl M, Gerber T, Küttinger M, Noack J, Fischer P, Pinkwart K, Tübke J. The role of phosphate additive in stabilization of sulphuric-acid based vanadium (V) electrolyte for allvanadium redox-flow batteries. J Power Sources 2017; 363:234–243. Doi: 10.1016/j.jpowsour.2017.07.100.

[18] Shi Y, Eze C, Xiong B, He W, Zhang H, Lim T M, Ukil A, Zhao J. Recent development of membrane for vanadium redox flow battery applications: A review. Appl Energy 2019; 238: 202–224. Doi: 10.1016/j.apenergy.2018.12.087.

[19] Chen D, Wang S, Xiao M, Meng Y. Synthesis and properties of novel sulfonated poly(arylene ether sulfone) ionomers for vanadium redox flow battery. Energ Conver Manage 2010; 51: 2816–2824. Doi: 10.1016/j.enconman.2010.06.019.

[20] Chen R, Bresser D, Saraf M, Gerlach P, Balducci A, Kunz S, Schrçder D, Passerini S, Chen J. A Comparative Review of Electrolytes for Organic-Material-Based Energy-Storage Devices Employing Solid Electrodes and Redox Fluids, Chem Sus Chem 2020; 13(9): 2205–2219. Doi: 10.1002/cssc.201903382.

[21] Gundlapalli R, Jayanti S. Performance characteristics of several variants of interdigitated flow fields for flow battery applications. J Power Sources 2020; 467: 228225. Doi: 10.1016/j.jpowsour.2020.228225.

[22] Chen F, Gao H, Chen H, Yan C. Evaluation of thermal behaviors for the multi-stack vanadium flow battery module. J Energy Storage 2020; 27:101081. Doi: 10.1016/j.est.2019.101081.

[23] Arenas L F, Ponce de Léon C, Walsh F C. Redox flow batteries for energy storage: their promise, achievements and challenges. Current Opinion in Electrochemistry 2019; 16: 117 –126: Doi: 10.1016/j.coelec.2019.05.007.

[24] Skyllas-Kazacos M, Menictas C, Kazacos M. Thermal Stability of Concentrated V(V) Electrolytes in the Vanadium Redox Cell. J Electrochem Soc 1996; 143(4): L86─L88; Doi:10.1149/1.1836609.

[25] Kim D, Jeonb J. A high-temperature tolerance solution for positive electrolyte of vanadium redox flow batteries. J Electroanalytical Chemistry 2017; 801: 92─97. Doi:10.1016/j.jelechem.2017.07.037.

[26] Tang A, Bao J, Skyllas-Kazacos M. Thermal modelling of battery configuration and self-discharge reactions in vanadium redox flow battery. J Power Sources 2012; 216: 489─501. Doi: 10.1016/j.jpowsour.2012.06.052.

[27] Skyllas-Kazacos M, Cao L, Kazacos M, Kausar N, Mousa A. Vanadium Electrolyte Studies for the Vanadium Redox Battery: A Review. Chem Sus Chem 2016; 9: 1521–1543. Doi:10.1002/cssc.201600102.

[28] Wang K, Zhang Y, Liu L, Xi J, Wu Z, Qiu X. Broad temperature adaptability of vanadium redox flow battery - Part 3: The effects of total vanadium concentration and sulfuric acid concentration. Electrochim Acta 2017; 259: 11─19. Doi: 10.1016/j.electacta.2017.10.148.

[29] Mousa A, Skyllas-Kazacos M. Effect of Additives on the Low-Temperature Stability of Vanadium Redox Flow Battery Negative Half-Cell Electrolyte. Chem Electro Chem, 2015; 2: 1742–1751. Doi: 10.1002/celc.201500233.

[30] Roe S, Menictas C, and Skyllas-Kazacos M. A High Energy Density Vanadium Redox Flow Battery with 3 M Vanadium Electrolyte. Journal of The Electrochemical Society 2016; 163: A5023–A5028. Doi: 10.1149/2.0041601jes.

[31] Kausar N, Mousa A, Skyllas-Kazacos M. The Effect of Additives on the High-Temperature Stability of the Vanadium Redox Flow Battery Positive Electrolytes. Chem Electro Chem 2016; 3: 276–282. doi: 10.1002/celc.201500453.

[32] Zhang J, Li L, Nie Z, Chen B, Vijayakumar M, Kim S, Wang W, Schwenzer B, Liu J, Yang Z. Effects of additives on the stability of electrolytes for all-vanadium redox flow batteries. Journal of Applied Electrochemistry, 2011, 41: 1215–1221; doi: 10.1007/s10800-011-0312-1.

[33] Arenas L, Ponce de Leòn C, Walsh F. Engineering aspects of the design, construction and performance of modular redox flow batteries for energy storage. J Energy Storage 2017; 11: 119–153. Doi: 10.1016/j.est.2017.02.007.

[34] Yan Y, Li Y, Skyllas-Kazacos M, Bao J. Modelling and simulation of thermal behavior of vanadium redox flow battery. J Power Sources 2016; 322: 116─128. Doi: 10.1016/j.jpowsour.2016.05.011.

[35] Wei Z, Zhao J, Xiong B. Dynamic electro-thermal modeling of all-vanadium redox flow battery with forced cooling strategies. Appl Energy 2014; 135: 1─10. Doi: 10.1016/j.apenergy.2014.08.062.

[36] Wu W, Wang S, Wu W, Chen K, Hong S, Lai Y. A critical review of battery thermal performance and liquid based battery thermal management. Energ Conver Manage 2019 182: 262–281. Doi: 10.1016/j.enconman.2018.12.051.

[37] Piłatowicz G, Budde-Meiwes H, Kowal J, Sarfert C, Schoch E, Konigsmann M, Sauer D U, Determination of the lead-acid battery's dynamic response using Butler-Volmer equation for advanced battery management systems in automotive applications. J Power Sources 2016; 331: 348–359. Doi: 10.1016/j. jpowsour.2016.09.066.

[38] Liu H, Wei Z, He W, Zhao J. Thermal issues about Li-ion batteries and recent progress in battery thermal management systems: A review. Energ Conver Manage 2017; 150: 304–330. Doi: 10.1016/j.enconman.2017.08.016.

[39] Yi-Huan Huang, Wen-Long Cheng, Rui Zhao. Thermal management of Li-ion battery pack with the application of flexible form-stable composite phase change materials. Energ Conver Manage 2019; 182: 9–20. Doi: 10.1016/j.enconman.2018.12.064.

[40] Shen M, Gao Q. System simulation on refrigerant-based battery thermal management technology for electric vehicles. Energ Conver Manage 2020; 203: 112176. Doi: 10.1016/j.enconman.2019.112176.

[41] Bhattacharjee A, Saha H. Development of an efficient thermal management system for Vanadium Redox Flow Battery under different charge-discharge conditions. Appl Energy 2018; 230: 1182–1192. Doi: 10.1016/j.apenergy.2018.09.056.

[42] Wei Z, Zhao J, Skyllas-Kazacos M, Xiong B. Dynamic thermal-hydraulic modeling and stack flow pattern analysis for all-vanadium redox flow battery. J Power Sources 2014; 260:89–99; Doi: 10.1016/j.jpowsour.2014.02.108.

[43] Tang A, Mc Cann J, Bao J, Skyllas-Kazacos M. Investigation of the effect of shunt current on battery efficiency and stack temperature in vanadium redox flow battery. J Power Sources 2013; 242: 349–356; doi.org/10.1016/j.jpowsour.2013.05.079.

[44] 2050 Long-term strategy -A Clean Planet for All, (2018) European Parliament. https://ec.europa.eu/clima/policies/strategies/2050_en; 2018 [accessed 26 August 2020].

[45] Skyllas-Kazacos M, Chakrabarti M H, Hajimolana S A, Mjalli F S, Saleem M. Progress in Flow Battery Research and Development. Journal of The Electrochemical Society 2011; 158: R55–R79. Doi: 10.1016/j.jpowsour.2013.05.079.

[46] Gildemeister Energy Solution. Use your own grid, http://www.retecon.co.za/wp-content/uploads/2015/06/CellCube-Brochure_web.pdf; [accessed 26 August 2020].

[47] Kaizuka T, Sasaki T. Evaluation of control maintaining electric power quality by use of rechargeable battery system. 2001 IEEE Power Engineering Society Winter Meeting. Conference Proceedings (Cat. No.01CH37194), Columbus, OH, USA, 2001; 1:88–93. Doi: 10.1109/PESW.2001.916870.

[48] Trovò A, Di Noto V, Guarnieri M. Time-domain study of the electric fast-response in a 9-kW vanadium redox flow battery. Submitted J Power Sources 2020.

[49] Oboroceanu D, Quill N, Lenihan C, Nì Eidhin D, Albu S P, Buckley D N. Effects of Temperature and Composition on Catholyte Stability in Vanadium Flow Batteries: Measurement and Modeling, J Electrochem Soc 2017; 164: A2101–A2109. Doi: 10.1149/2.1401709jes.

[50] Guarnieri M, Trovò A, D'Anzi A, Alotto P. Developing vanadium redox flow technology on a 9-kW 26-kWh industrial scale test facility: Design review and early experiments, Appl Energy. 2018; 230:1425–1434. Doi: 10.1016/j.apenergy.2018.09.021.

[51] Guarnieri M, Trovò A, Marini G, Sutto A, Alotto P, High current polarization tests on a 9 kW vanadium redox flow battery, J Power Sources 2019; 431:239–249. Doi: 10.1016/j.jpowsour.2019.05.035.

[52] Trovò A. Battery management system for industrial-scale vanadium redox flow system batteries: features and operation. J Power Sources, 2020; 465:228229. Doi: 10.1016/j.jpowsour.2020.228229.

[53] Trovò A, Marini G, Sutto G, Alotto P, Giomo M, Moro F, Guarnieri M. Standby thermal model of a vanadium redox flow battery stack with crossover and shunt-current effects. Appl Energy 2019; 240: 893–906. Doi: 10.1016/j.apenergy.2019.02.067.

[54] Trovò A, Saccardo A, Giomo M, Guarnieri M. Thermal modeling of industrial-scale vanadium redox flow batteries in high-current operations. J Power Sources 2019, 424: 204–214. Doi: 10.1016/ j.jpowsour.2019.03.080.

[55] Pugach M, Kondratenko M, Briola S, Bischi A. Zero dimensional dynamic model of vanadium redox flow battery cell incorporating all modes of vanadium ions crossover, Applied energy 2018; 226:560–569. Doi: 10.1016/j.apenergy.2018.05.124.

[56] Darling M R, Weber Z A, Tucker C M, Perry L M. The Influence of Electric Field on Crossover in Redox-Flow Batteries. J Electrochem Soc 2016; 163: A5014–A5022. Doi: 10.1149/2.0031601jes.

[57] Lawton S J, Jones A, Zawodzinski T. Concentration Dependence of VO2+ Crossover of Nafion for Vanadium Redox Flow Batteries. J Electrochem Soc 2013; 160: A697–A702. Doi: 10.1149/2.004306jes.

[58] Tang A, Bao J, Skyllas-Kazacos M. Dynamic modelling of the effects of ion diffusion and side reactions on the capacity loss for vanadium redox flow battery. J Power Sources 2011; 196: 10737–10747. Doi: 10.1016/j.jpowsour.2011.09.003.

[59] Roznyatovskaya N, Herr T, Küttinger M, Fühl M, Noack J, Pinkwart K, Tübke J. Detection of capacity imbalance in vanadium electrolyte and its electrochemical regeneration for all-vanadium redox-flow batteries. J Power Sources 2016; 302: 79–83. Doi: 10.1016/j.jpowsour.2015.10.021.

[60] Sun C, Zlotorowicz A, Nawn G, Negro E, Bertasi F, Pagot G, Vezzù K, Pace G, Guarnieri M, Di Noto V. [ Nafion/(WO 3) x] hybrid membranes for vanadium redox flow batteries. Solid State Ionics June 2018; 319: 110–116. Doi: 10.1016/j.ssi.2018.01.038.

[61] Oldenburg J F, Schmidt J T, Gubler L. Tackling capacity fading in vanadium flow batteries with amphoteric membranes. J Power Sources 2017; 368: 68 –72. Doi: 10.1016/j.jpowsour.2017.09.051.

[62] Trovò A, Picano F, Guarnieri M. Comparison of energy losses in a 9 kW vanadium redox flow battery. J Power Sources 2019; 440: 227144. Doi: 10.1016/j.jpowsour.2019.227144.

[63] Li Y, Skyllas-Kazacos M, Bao J. A dynamic plug flow reactor model for vanadium redox flow battery cell. J Power Sources 2016; 311: 57–67. Doi: 10.1016/j.jpowsour.2016.02.018.

[64] Zhang Y, Zhao J, Wang P, Skyllas-Kazacos M, Xiong B, Badrinarayanan R. A comprehensive equivalent circuit model of all-vanadium redox flow battery for power system analysis. J Power Sources, 2015; 290:14–24. Doi: 10.1016/j.jpowsour.2015.04.169.

[65] Guarnieri M, Trovò A, Picano F. Enhancing the efficiency of kW-class vanadium redox flow batteries by flow factor modulation: an experimental method. Appl Energy 2020; 262:114532. Doi: 10.1016/j.apenergy.2020.114532.

[66] Khazaeli A, Vatani A, Tahouni N, Panjeshahi M H. Numerical investigation and thermodynamic analysis of the effect of electrolyte flow rate on performance of all vanadium redox flow batteries. J Power Sources 2015; 293: 599–612. Doi: 10.1016/j.jpowsour.2015.05.100.

[67] Xiong B, Zhao J, Tseng K J, Skyllas-Kazacos M, Lim T M, Zhang Y. Thermal hydraulic behavior and efficiency analysis of an all-vanadium redox flow battery. J Power Sources 2013; 242: 314–324. Doi: 10.1016/j.jpowsour.2013.05.092.

[68] Trovò A, Picano F, Guarnieri M. Maximizing vanadium redox flow battery efficiency: Strategies of flow rate control, in: 2019 IEEE 28th International Symposium on Industrial Electronics (ISIE), IEEE, 2019, 1977-1982. Doi: 10.1109/ISIE.2019.8781152.